ACS APPLIED MATERIALS & INTERFACES

Research Article

www.acsami.org

Triple Cathode Buffer Layers Composed of PCBM, C_{60}, and LiF for High-Performance Planar Perovskite Solar Cells

Xiaodong Liu,[†] Hao Yu,[†] Li Yan,[†] Qingqing Dong,[†] Qun Wan,[†] Yi Zhou,*[,†] Bo Song,*[,†] and Yongfang Li*[,†,‡]

[†]Laboratory of Advanced Optoelectronic Materials, College of Chemistry, Chemical Engineering and Materials Science, Soochow University, Suzhou, Jiangsu 215123, China

[‡]Beijing National Laboratory for Molecular Sciences, Institute of Chemistry, Chinese Academy of Sciences, Beijing 100190, China

Supporting Information

ABSTRACT: In this paper, triple cathode buffer layers (CBLs) composed of phenyl-C_{61}-butyric acid methyl ester (PCBM), C_{60}, and LiF layers were introduced into the planar p−i−n perovskite solar cells (p−i−n PSCs) with a device structure of ITO/PEDOT:PSS/$CH_3NH_3PbI_{3-x}Cl_x$/CBLs/Al. For comparison, a single CBL of PCBM and a double CBL of PCBM/LiF were also investigated in the p−i−n PSCs. On the basis of the PCBM buffer layer, the addition of a thin LiF layer facilitated the charge collection process and led to the dramatic improvement of the power conversion efficiency (PCE) of the PSCs up to 14.69% under an illumination of AM 1.5G, 100 mW/cm^2, which is to date one of the highest efficiencies of the p−i−n PSCs. By further insertion of a C_{60} layer between PCBM and LiF in the triple CBLs, a PCE of 14.24% was obtained, and more importantly, the PCBM/C_{60}/LiF triple CBLs are very helpful for improving the stability of the devices and making the LiF layer less thickness-sensitive for achieving high performances of the p−i−n PSCs.

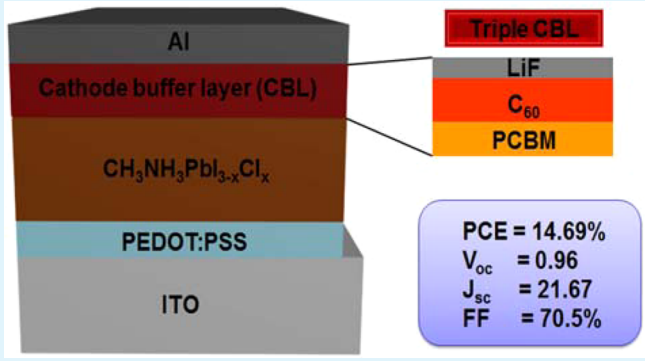

KEYWORDS: *planar perovskite solar cells, cathode buffer layers, PCBM/C_{60}/LiF triple CBLs, $CH_3NH_3PbI_{3-x}Cl_x$, stability*

1. INTRODUCTION

Organic−inorganic hybrid perovskite materials, for application in solar cells, have attracted considerable attention recently because of their unique properties, such as high absorption coefficient, excellent ambipolar charge mobility, and small exciton binding energy.[1−15] Over the past 5 years, the power conversion efficiency (PCE) of organometal halide perovskite solar cells (PSCs) has skyrocketed from 3.8% to 20.1%, approaching the efficiency of commercialized crystalline Si solar cells.[1,2,16−30] Although first implemented in dye-sensitized solar cells based on mesoporous structures, perovskites have also been applied to planar heterojunction solar cells, which are adaptable to low-temperature solution processes.[1,14,15,31−34] The configuration of the planar heterojunction solar cell based on perovskite is quite similar to that of organic photovoltaic cells.[35−39]

According to the indium−tin oxide (ITO) electrode used as the anode or cathode, we can define the planar PSCs with ITO as the anode as p−i−n PSCs and that with ITO as the cathode as n−i−p PSCs.[34] The n−i−p PSCs usually employing compact TiO_2 as the cathode buffer layer (CBL) have demonstrated rather high performance.[40] However, the compact TiO_2 layer requires high-temperature sintering at 450−500 °C. Moreover, the n−i−p PSCs show an anomalous current−voltage (I−V) hysteresis phenomenon depending on the scan direction and scan rate.[41−45] As an alternative of n−i−p PSCs, the p−i−n PSCs can be fabricated at relatively low temperature, and the hysteresis problem can also be solved. Recently, special attention has been given to the p−i−n PSCs. Nevertheless, the efficiency of p−i−n PSCs is still lower than that of n−i−p PSCs. Also, as a common problem of both types of PSCs, the device stability is of crucial importance for the researchers.

For the planar heterojunction PSCs, apart from the perovskite photoactive layer, the buffer layers sandwiched between the photoactive layer and the electrodes are crucial to obtaining the highly efficient and stable solar cells.[46,47] LiF is a widely used CBL in polymer solar cells between the photoactive layer and the Al cathode.[48] Very recently, Seo et al.[11] introduced a very thin layer of LiF (0.5 nm) into the p−i−n PSC based on $CH_3NH_3PbI_3$ and gained a PCE as high as 14.1%. Ouyang et al. also realized the efficiency enhancement of planar PSCs by adding zwitterion/LiF double interlayers for electron collection.[49] LiF is known as an electrical insulator, and the thickness is usually controlled to less than 2 nm in

Received: January 16, 2015
Accepted: March 5, 2015
Published: March 5, 2015

DOI: 10.1021/acsami.5b00468
ACS Appl. Mater. Interfaces 2015, 7, 6230−6237

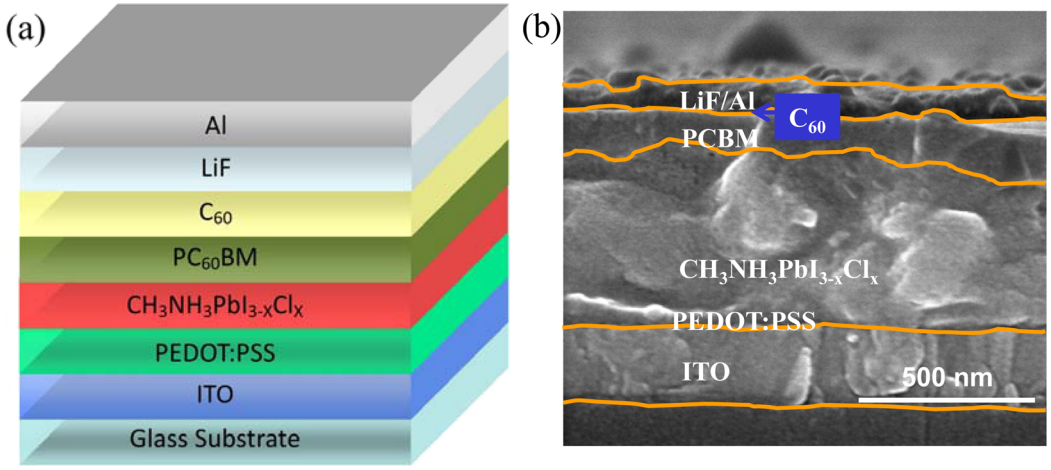

Figure 1. (a) Schematic illustration and (b) cross-sectional SEM image of the PSC. The thicknesses of PEDOT:PSS, $CH_3NH_3PbI_{3-x}Cl_x$, and PCBM are approximately 40, 450, and 100 nm, respectively.

polymer solar cells for an optimal performance. Compared with the roughness of the perovskite, such a thickness is rather small and very difficult to precisely control during thermal deposition. A tolerant thickness would be necessary for practical applications.

Gao et al. and Liu et al. reported that the C_{60}:LiF composite deposited by coevaporation[50] or the stacks of C_{60}/LiF prepared via layer-by-layer deposition[51] can greatly enhance the stability of conventional polymer solar cells based on a P3HT:PCBM blend. Inspired by their work, we introduced both of the C_{60} and LiF buffer layers into the p−i−n PSCs, with a device architecture of ITO/PEDOT:PSS/$CH_3NH_3PbI_{3-x}Cl_x$/PCBM/C_{60}/LiF/Al [where PEDOT:PSS is poly(3,4-ethylenedioxythiophene):poly(styrenesulfonic acid)]. Including the PCBM buffer layer, PCBM/C_{60}/LiF makes up triple CBLs in this work. It was found that the champion PCE of the p−i−n PSC with PCBM/LiF (1 nm) double CBLs reached 14.69%, which is slightly higher than the PCE reported in ref 11. Also, the p−i−n PSC with triple CBLs of PCBM/C_{60} (15 nm)/LiF (1 nm) demonstrated a PCE of 14.24%. More importantly, with the triple CBLs, the stability of the p−i−n PSC was dramatically improved. 80% of the PCE remained over 19 days of storage in the glovebox (including 5 min air exposure) for the device with triple CBLs versus 12% remaining over 15 days for the device with PCBM/LiF double CBLs. Moreover, by the introduction of a C_{60} buffer layer, the thickness of LiF needs not to be so critically thin. Even when the thickness of LiF was increased to 5 nm, a PCE of 13.77% was still obtained, which is very important for the fabrication and device performance reproduction of PSCs.

2. EXPERIMENTAL SECTION

Preparation of the Perovskite Precursor. Methylammonium iodide (MAI) was synthesized according to the literature by stoichiometrically reacting methylamine with hydroiodic acid at 0 °C with stirring for 2 h.[9] The precipitate was washed by dissolving in a minimum amount of ethanol and then adding in a large amount of diethyl ether. The precipitate was collected by filtration. The procedure was repeated three times to get pure MAI. The resulting product (white powder) was dried at 60 °C. The perovskite precursor was prepared by mixing MAI and $PbCl_2$ (99.999%, Alfa) in a molar ratio of 3:1 in anhydrous *N*,*N*-dimethylformamide (DMF; 99.8%, Acros), and the final concentration of the perovskite was controlled to approximately 40 wt %. To the mixture was added approximately 1% 1,8-diiodooctane (DIO; volume fraction of DMF). The mixture was then stirred overnight at 60 °C and filtered through a 0.45 μm filter right before device fabrication. The perovskite precursor was stored in a glovebox.

Fabrication of Planar p-i-n PSCs. As shown in Figure 1, the typical device configuration was ITO/PEDOT:PSS/$CH_3NH_3PbI_{3-x}Cl_x$/CBLs/Al, where the CBLs were PCBM (single CBL), PCBM/LiF (double CBLs), and PCBM/C_{60}/LiF (triple CBLs). The experimental details are illustrated as follows. ITO-coated glass (CSG Holding Co., Ltd., 10 Ω/sq) substrates were cleaned sequentially with detergent, deionized water, acetone, ethanol, and isopropyl alcohol under sonification for 10 min each and then treated with oxygen plasma for 15 min to generate a hydrophilic surface. The PEDOT:PSS solution (Clevious P VP AI 4083) was filtered and spin-coated onto the cleaned ITO substrates at 2000 rpm for 50 s, and then the ITO substrates were baked at 150 °C for 20 min in air. The following operation was carried out in a glovebox filled with nitrogen. Every time before use, the 40 wt % $CH_3NH_3PbI_{3-x}Cl_x$/DIO precursor solution was filtered by running through a 0.45 μm filter and then spin-coated on top of PEDOT:PSS at 3000 rpm for 50 s. The ITO substrates with the perovskite precursor were thermally annealed at 105 °C for 38 min. PCBM with a concentration of 15 mg/mL in chloroform was then spin-coated atop the perovskite layer at 1200 rpm for 60 s. Finally, C_{60}, LiF, and Al electrode were sequentially deposited by thermal evaporation at a base pressure of 1×10^{-4} Pa. The deposition rate and film thickness were monitored with a quartz crystal sensor. A shadow mask was closely covered on the sample to define an active area of 0.2 cm × 0.2 cm during Al deposition.

Characterization. The current density−voltage (*J*−*V*) characteristics were measured using a Keithley 2400 source meter unit under simulated Air Mass 1.5 Global (AM 1.5G) solar illumination with an intensity of 100 mW/cm^2. The solar illumination was calibrated by a standard Si solar cell. The measurements were conducted inside the glovebox (both O_2 and H_2O < 1 ppm). The incident photon-to-current conversion efficiency (IPCE) was measured by a solar cell spectral response measurement system (Enli Technology Co., Ltd., QE-R3011). The light intensity was calibrated using a single-crystal Si photovoltaic cell as a reference. The alternating-current (ac) impedance spectroscopy (ACIS) measurements were performed on a IM6 electrochemical workstation (Zahner Zennium, Germany) in dark conditions, with an applied bias of 0.95 V. An ac signal with a root-mean-square (rms) amplitude of 10 mV over the frequency range of 4 MHz to 0.3 Hz was adopted during the measurement. The impedance parameters were determined by fitting the impedance spectra using *Z-view* software. During evaluation of the stability, the PSCs were stored and measured in the glovebox, while the cells were taken out of the glovebox and exposed to ambient atmosphere for about 5 min during the ACIS measurements. Atomic force microscopy (AFM) images were captured on a Multimode 8 microscope (Bruker, Santa Barbara, CA) with peak force quantitative nanomechanical mode.

DOI: 10.1021/acsami.5b00468
ACS Appl. Mater. Interfaces 2015, 7, 6230−6237

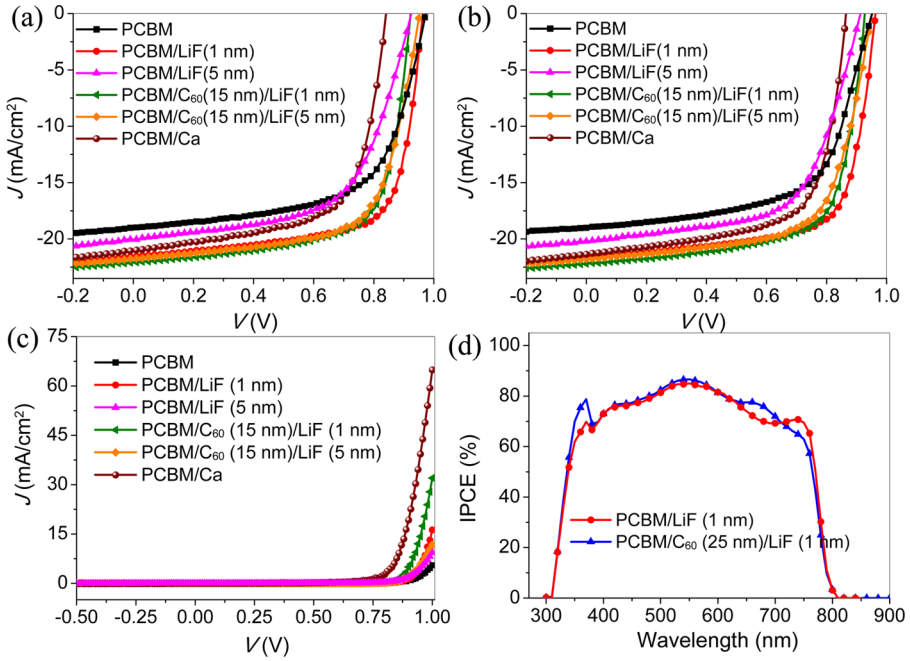

Figure 2. (a) FS and (b) RS $J-V$ curves of the p−i−n PSCs with different CBLs under an illumination of AM 1.5G, 100 mW/cm^2. (c) $J-V$ characteristics measured in the dark. (d) IPCE spectra of the PSCs with PCBM/LiF (1 nm) and PCBM/C_{60} (25 nm)/LiF (1 nm) as CBLs.

Scanning electron microscopy (SEM) observations were performed on a S-4700 microscope (Hitachi, Japan) operating at 15 kV. X-ray diffraction (XRD) was carried out using an X'Pert-Pro MRD diffractometer (Panalytical).

3. RESULTS AND DISCUSSION

3.1. Photovoltaic Performance of the p−i−n PSCs.

First, we were wondering if the p−i−n PSCs also have hysteresis behavior like the n−i−p PSCs reported in the literature. In order to unravel this question, the $J-V$ curves were recorded by alternating the scan directions. For convenience of description, scanning the bias from low voltage to high voltage is denoted by forward scan (FS), and that from high voltage to low voltage is called reverse scan (RS). The $J-V$ curves of the PSCs with different CBLs were measured with a 200 ms delay after each 10 mV voltage step. The results are shown in Figure 2a,b. The corresponding photovoltaic parameters of the devices are listed in Table 1. It is clearly shown by the two plots, as well as the photovoltaic parameters, that the PCEs obtained from FS and RS are quite close to each other for the different PSCs with different CBLs. The results indicate that the photovoltaic performance data are more reliable for the p−i−n PSCs. In the following, the photovoltaic parameters mentioned in the discussion are obtained from RS.

It can be seen from Table 1 that the PCE of the PSC with a PCBM single CBL is 11.20%. After the introduction of a LiF (1 nm) layer between PCBM and the Al cathode in the device with PCBM/LiF double CBLs, both the short-circuit current density (J_{sc}) and the fill factor (FF) increased dramatically and, as a consequence, the PCEs reached as high as 14.69%. To further confirm the above results, the $J-V$ curves of the device with PCBM/LiF(1 nm) CBLs were measured with various delay times from 5 to 500 ms after each 10 mV voltage step (see the $J-V$ curves in Figure S1 in the Supporting Information, SI). The $J-V$ curves, from either FS or RS, are independent of the delay times, indicating efficient charge collection within the perovskite layer. To find out the reasons

Table 1. Photovoltaic Performance of the p−i−n PSCs with Different CBLs

	CBL	J_{sc} (mA/cm^2)	V_{oc} (V)	FF (%)	PCE (%)	R_s (Ω cm^2)	R_{sh} (Ω cm^2)
FS	PCBM	19.04	0.97	62.2	11.52	8.12	333.72
	PCBM/LiF (1 nm)	21.60	0.96	70.5	14.65	3.15	367.57
	PCBM/LiF (5 nm)	20.04	0.92	59.7	11.07	8.85	290.49
	PCBM/C_{60} (15 nm)/LiF (1 nm)	22.08	0.92	69.2	14.09	3.12	357.79
	PCBM/C_{60} (15 nm)/LiF (5 nm)	21.74	0.95	66.6	13.79	5.68	370.13
	PCBM/Ca	21.03	0.84	65.0	11.50	3.75	245.59
RS	PCBM	19.01	0.95	61.9	11.20	9.61	329.33
	PCBM/LiF (1 nm)	21.67	0.96	70.5	14.69	3.28	378.24
	PCBM/LiF (5 nm)	20.19	0.91	61.5	11.33	9.91	306.00
	PCBM/C_{60} (15 nm)/LiF (1 nm)	22.21	0.93	69.2	14.24	3.14	368.53
	PCBM/C_{60} (15 nm)/LiF (5 nm)	21.76	0.95	66.6	13.77	5.94	372.46
	PCBM/Ca	21.36	0.86	66.6	12.30	3.09	269.62

for the increase of J_{sc} and FF, the series resistances (R_s) and shunt resistances (R_{sh}) were calculated from the slope of the photo $J-V$ curves at 0 mA/cm^2 and 0 V, respectively. The results are also listed in Table 1. The decrease of R_s and the increase of R_{sh} after insertion of LiF (1 nm) can explain the dramatic improvement of J_{sc} and FF. The decreased R_s can also be verified by the dark $J-V$ characteristics of the devices, as shown in Figure 2c. The relatively larger injection current at positive bias (e.g., 1.0 V) of the device with LiF (1 nm) CBL agrees well with the lower R_s. The formation of a good ohmic contact between PCBM and Al electrode due to the strong dipole moment of LiF should be responsible for the significant reduction of R_s. With regard to this aspect, further discussions are conducted by ACIS later in this paper.

The slight increase of R_{sh} can be explained by the nature of LiF, which is known as an insulator with a wide band gap (~12 eV). This makes LiF a good hole-blocking layer to reduce the current leakage in the device. For the same reason, further

DOI: 10.1021/acsami.5b00468
ACS Appl. Mater. Interfaces 2015, 7, 6230−6237

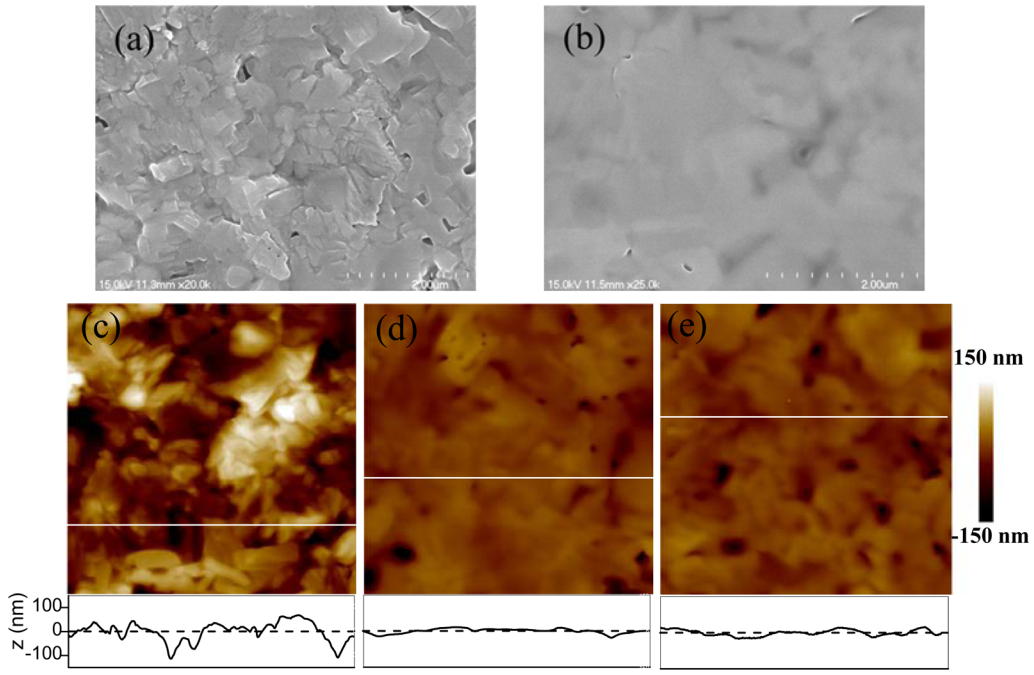

Figure 3. Top-view SEM images of (a) the $CH_3NH_3PbI_{3-x}Cl_x$ film and (b) the PCBM@$CH_3NH_3PbI_{3-x}Cl_x$ film. AFM height images and corresponding sectional profiles of (c) $CH_3NH_3PbI_{3-x}Cl_x$, (d) PCBM@$CH_3NH_3PbI_{3-x}Cl_x$, and (e) C_{60}@PCBM@$CH_3NH_3PbI_{3-x}Cl_x$. The rms values calculated from parts c–e are 45.7, 17.3, and 17.8 nm, respectively. The scanning range of the AFM images is 5 μm × 5 μm.

increasing the thickness of LiF will inevitably lead to an increase of R_s, as well as a decrease of FF. This assertion is echoed by the decrease of the PCEs of the devices with an increase in the thickness of LiF to 5 nm, as shown by the photovoltaic performance in Figure 2a,b. In addition, the variation trend of the dark current density indicated by the dark J–V curves in Figure 2c is also consistent with the device performance.

The insertion of C_{60} between PCBM and LiF [i.e., PCBM/C_{60} (25 nm)/LiF (1 nm) triple CBLs] led to a PCE of 13.59%. The value is slightly lower than that of the solar cells with PCBM/LiF (1 nm) double CBL. The decrease of the PCE, after insertion of C_{60}, can be ascribed to the drop of V_{oc} (see Table S1 in the SI). To optimize the performance of the PSCs with PCBM/C_{60}/LiF triple CBLs, we fixed the LiF thickness at 1 nm and then varied the thickness of C_{60} from 10 to 15 to 25 nm (the photovoltaic performances are listed in Figure S2a,b in the SI). When the thickness of C_{60} was 15 nm, the PCEs reached the maximum value of 14.24%. This is close to the PCE of the PSC with PCBM/LiF (1 nm) double CBLs. To check the reproducibility of the results, we repeated the experiments on fabricating and characterizing the p–i–n PSCs. Statistical data on a batch of five devices for each type are shown in Table S2 in the SI. The PSCs with PCBM/C_{60} (15 nm)/LiF (1 nm) triple CBLs exhibited an average PCE of 13.97% with a standard derivation of 0.3%, indicating very good reproducibility.

Herein, the IPCE spectra were employed to explain J_{sc} of the devices with and without a C_{60} buffer layer. As shown in Figure 2d, although the peak values of the devices with and without a C_{60} interlayer both approach 85% at 550 nm, the shapes of the IPCE curves at 630–780 nm are significantly different. This can be attributed to the optical spacer effect from the C_{60} layer according to the theory proposed by Yip et al.[52] It is worth noting that the integrated IPCE values are in good agreement with the corresponding J_{sc} obtained from the J–V curves.

As described above in this research, when using PCBM/LiF as the CBL, the thickness of LiF has to be thin (~1 nm) for a high efficiency, and increasing the thickness from 1 to 5 nm resulted in a drastic decrease of the PCE from 14.69% to 11.33%. Here we found that after introducing the C_{60} layer the thickness of LiF is not necessarily thin and allows a relatively wide range of thickness for high efficiencies of the devices. As shown in Table 1, the PSC with PCBM/C_{60} (15 nm)/LiF (5 nm) triple CBLs showed a PCE of 13.77%, a moderate decrease of PCE compared with 14.24% but significantly higher than that of the solar cell with PCBM/LiF (5 nm) double CBLs. This improvement in the PCE is mainly attributed to the enhanced J_{sc} and FF, which resulted from reduced R_s due to the introduction of C_{60}. R_s of the device with PCBM/C_{60} (15 nm)/LiF (5 nm) triple CBLs was 5.94 Ω cm^2, much lower than that of the device with PCBM/LiF (5 nm) double CBLs. The reduced R_s indicates a better electrical conductivity of the C_{60}/LiF (5 nm) bilayer compared with the single LiF (5 nm) layer. It has been proven that intermixing occurs at the C_{60}/LiF interface when 5-nm-thick LiF was deposited on top of the C_{60} layer.[51] This leads to good electrical conductivity of the C_{60}/LiF (5 nm) bilayer considering the percolation path formed by the C_{60} molecules.

The low-work-function metal Ca is an often used CBL in polymer solar cells. For comparison, Ca was also introduced into the p–i–n PSCs. It turns out that the device with PCBM/Ca double CBLs had a PCE of 12.30%, a little bit higher than that with a PCBM single CBL. As shown in Figure 2a,b, the incorporation of the Ca CBL resulted in significant improvement of J_{sc} and moderate improvement of FF but a drastic decrease of V_{oc} in comparison with the PCBM single CBL device. The enhancement in J_{sc} and FF can be attributed to the reduction of R_s, which facilitates electron transport and collection.

3.2. Morphology Studies. The performance of the PSCs is correlated with the morphology of the active layer, i.e., the crystalline structure of the perovskite. As shown by the top-view SEM image in Figure 3a, $CH_3NH_3PbI_{3-x}Cl_x$ formed sharply

DOI: 10.1021/acsami.5b00468
ACS Appl. Mater. Interfaces 2015, 7, 6230–6237

faceted crystalline domains with sizes of a few hundreds of nanometers, and the nanocrystals were closely connected. Generally, a uniform and highly crystallized film usually promises a high performance of the PSCs.[9,11] After a PCBM buffer layer was capped (Figure 3b), the surface became rather smooth and homogeneous. To obtain the *z*-direction information on the films, AFM measurement was carried out, and the images and corresponding section analysis are shown in Figure 3c–e. It can be seen clearly that the topologies of $CH_3NH_3PbI_{3-x}Cl_x$ and PCBM@$CH_3NH_3PbI_{3-x}Cl_x$ have trends similar to those shown by SEM. The surface roughnesses calculated by the rms of the height data in the scan range of 5 μm × 5 μm were 45.7 and 17.3 nm for $CH_3NH_3PbI_{3-x}Cl_x$ and PCBM@$CH_3NH_3PbI_{3-x}Cl_x$, respectively. With coverage of PCBM, the surface roughness was significantly decreased, as also was evidenced by the corresponding sectional profiles. The smoother surface suggests a better interfacial contact between PCBM and the top cathode. Additionally, full coverage of PCBM on the perovskite film can block the direct contact between the cathode and the active layer and thus minimize the current leakage.[11] Nevertheless, further deposition of C_{60} (15 nm) has very little contribution to the surface topology or roughness. This can be ascribed to the fact that (1) thermal evaporation gives an equal regional thickness of C_{60} and (2) the thickness of the C_{60} layer is too small to affect the total roughness.

3.3. ACIS Studies of the p–i–n PSCs. To further investigate the effect of CBLs on the interfacial resistance of the devices, ACIS of the p–i–n PSCs was measured and analyzed. Figure 4a shows Nyquist plots of the p–i–n PSCs with

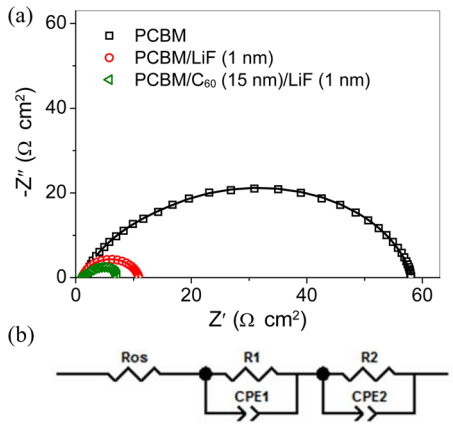

Figure 4. (a) Nyquist plots and fitting curves of the PSCs. ACIS was measured in the dark and near the V_{oc} condition (0.95 V). (b) Equivalent circuit.

different CBLs measured in the dark and near the V_{oc} condition (0.95 V). The impedance data were analyzed by fitting to an equivalent electrical circuit, as shown in Figure 4b. The equivalent circuit consists of a series connection of an ohmic series resistance (R_{os}) and two parallel resistance–constant phase elements (R||CPE). R_{os} is mainly contributed by the conducting wires, contacts, and sheet resistance of the collecting electrodes,[53] and CPE is used to describe a nonideal capacitor with the capacitive contribution CPE-T and the quality factor CPE-P.[54] The parameters obtained by fitting the impedance spectra are listed in Table 2. All of the devices have similar R_{os}, which is reasonable because of the similar configurations of the solar cells. R_1||CPE_1 and R_2||CPE_2 correspond to the semicircles with high and low frequencies

Table 2. Parameters of the Equivalent Circuit for the p–i–n PSCs with Different CBLs

CBL	R_{os} (Ω cm²)	R_1 (Ω cm²)	CPE_1-T (μF cm^{-2})	CPE_1-P	R_2 (Ω cm²)	CPE_2-T (μF cm^{-2})	CPE_2-P
PCBM	1.89	5.76	0.17	0.96	50.60	0.46	0.86
PCBM/LiF	1.41	0.31	5.81	1.11	9.14	0.21	0.96
PCBM/C_{60}/LiF	1.79	1.73	0.07	1.04	3.64	0.14	1.02

and are assigned to the photoactive layer and buffer interlayer, respectively.[55] R_2 of the p–i–n PSCs with PCBM, PCBM/LiF (1 nm), and PCBM/C_{60} (15 nm)/LiF (1 nm) CBLs were 50.60, 9.14, and 3.64 Ω cm², respectively. The variation trend is consistent with that of R_s extracted from the photo *J*–*V* curves (Table 1). For a parallel comparison, R_s was reevaluated from the dark *J*–*V* curve at around 0.95 V. The values were 18.18, 5.75, and 3.34 Ω cm². The three different methods all prove that the introduction of the C_{60} layer greatly decreases R_s, which makes a rational explanation for the higher J_{sc} of the corresponding device.

3.4. Stability of the p–i–n PSCs. In addition to the PCE, the stability is another important aspect that needs to be improved for the practical application of PSCs. We found that the insertion of the C_{60} layer is helpful for enhancing the stability of the devices. Figure 5 shows the normalized

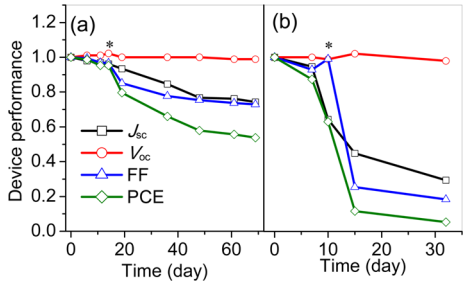

Figure 5. Photovoltaic characteristics normalized by their initial values, for the p–i–n PSCs with (a) PCBM/C_{60} (15 nm)/LiF (1 nm) and (b) PCBM/LiF (1 nm) CBLs, as a function of the storage time in the glovebox. Asterisks denote the data points of air exposure for ~5 min.

photovoltaic characteristics of the devices with PCBM/C_{60}/LiF triple CBLs and PCBM/LiF double CBLs as a function of the storage time in the glovebox (O_2 and H_2O < 1 ppm). As shown in Figure 5, the former maintained 95% of its initial efficiency after being stored in the glovebox for 14 days, while the latter retained only 63% after 10 days. Both of them were quite unstable when exposed in air at the data points denoted by asterisks, even for a rather short time. After exposure in air, a drastic decrease of the performance can be observed. It is worth noting that the device with the C_{60} layer is much stable than that without. The stability is also evidenced in the continuous storage after air exposure. With PCBM/LiF double CBLs, merely 12% of the PCE remained over 15 days of storage in the glovebox (including 5 min of air exposure). With triple CBLs, the stability of the p–i–n PSC was dramatically improved. Nearly 80% of the PCE remained over 19 days (including 5 min of air exposure). These results imply that the C_{60} buffer layer may have a blocking effect to water and/or oxygen to some extent, which is greatly helpful to improving the device stability.

From Figure 5, it can be seen that the PCE decay for both devices is dominated by the decline in J_{sc} and FF, while V_{oc}

DOI: 10.1021/acsami.5b00468
ACS Appl. Mater. Interfaces 2015, 7, 6230–6237

remains remarkably stable. This phenomenon is especially notable after air exposure for ~5 min. To gain more insight into the degradation process, dynamic evolution of the $J-V$ curves as a function of the storage time in the glovebox for both devices with PCBM/C_{60}/LiF and PCBM/LiF CBLs is presented in Figure S3 in the SI. S-shaped kinks were observed near V_{oc} in the $J-V$ curves for both devices after exposure to air. The kinks became more pronounced with increasing storage time, consequently resulting in decreased J_{sc} and FF. The appearance of the S-shaped kinks implies the existence of large R_s. Considering that no color change was observed for the perovskite films during aging, the significant increase in R_s should not be ascribed to the perovskite decomposition. Therefore, the substantially enhanced R_s most likely originated from the increased contact resistance between the perovskite and the PCBM CBL. The incorporation of the C_{60} layer between the PCBM and LiF layers provides good protection for the perovskite/PCBM interface by blocking water and/or oxygen, which leads to the slower increase of R_s (less severe kink) with the storage time and thus the improvement of the device stability.

4. CONCLUSION

In this study, we found that the performance of the p−i−n PSC, different from the n−i−p PSC, shows a scanning-direction-independent feature. With the introduction of a very thin layer of LiF (1 nm), the performance of the p−i−n PSCs was significantly improved. After insertion of a C_{60} layer (typically 15 nm) between the PCBM and LiF layers, the LiF layer is no longer thickness-sensitive until 5 nm for high device performance. Champion PCEs of 14.24% and 14.69% were obtained for PSCs with PCBM/C_{60}/LiF triple CBLs and PCBM/LiF double CBLs, respectively. These efficiencies are among the highest PCEs reported to date for the planar p−i−n PSCs based on the device configuration of ITO/PEDOT:PSS/$CH_3NH_3PbI_{3-x}Cl_x$/CBLs/Al. More importantly, the incorporation of the C_{60} layer with PCBM and LiF CBLs dramatically enhanced the stability of the p−i−n PSCs. We believe that the results of this study may pave the way toward achieving more efficient and stable p−i−n PSCs, and this idea can be expanded to systems featuring other types of perovskite materials.

■ ASSOCIATED CONTENT

Supporting Information

$J-V$ characteristics of the planar p−i−n PSCs with PCBM/LiF (1 nm) CBLs (Figure S1), effect of the C_{60} layer thickness on the $J-V$ curves and the photovoltaic performance of the p−i−n PSCs with PCBM/C_{60}/LiF CBLs (Figure S2 and Table S1), average photovoltaic performance parameters of the p−i−n PSCs with different CBLs (Table S2), and evolution of the $J-V$ curves as a function of the storage time in the glovebox for the PSCs with PCBM/C_{60} (15 nm)/LiF (1 nm) and PCBM/LiF (1 nm) CBLs (Figure S3). This material is available free of charge via the Internet at http://pubs.acs.org.

■ AUTHOR INFORMATION

Corresponding Authors

*E-mail: yizhou@suda.edu.cn.
*E-mail: songbo@suda.edu.cn.
*E-mail: liyf@iccas.ac.cn.

Notes

The authors declare no competing financial interest.

■ ACKNOWLEDGMENTS

The authors thank Yue Zhao for her help in AFM measurement. This work was supported by the National Natural Science Foundation of China (Grants 21204054, 51303118, and 91333204), the Natural Science Foundation of Jiangsu Province (Grant BK20130289), the Ph.D. Programs Foundation of Ministry of Education of China (Grant 20133201120008), the Priority Academic Program Development of Jiangsu Higher Education Institutions, the Scientific Research Foundation for Returned Scholars, Ministry of Education of China, and Beijing National Laboratory for Molecular Sciences.

■ REFERENCES

(1) Kojima, A.; Teshima, K.; Shirai, Y.; Miyasaka, T. Organometal Halide Perovskites as Visible-Light Sensitizers for Photovoltaic Cells. *J. Am. Chem. Soc.* **2009**, *131*, 6050−6051.
(2) Snaith, H. J. Perovskites: The Emergence of a New Era for Low-Cost, High-Efficiency Solar Cells. *J. Phys. Chem. Lett.* **2013**, *4*, 3623−3630.
(3) Ku, Z.; Rong, Y.; Xu, M.; Liu, T.; Han, H. Full Printable Processed Mesoscopic $CH_3NH_3PbI_3/TiO_2$ Heterojunction Solar Cells with Carbon Counter Electrode. *Sci. Rep.* **2013**, *3*, 3132.
(4) Park, N.-G. Organometal Perovskite Light Absorbers toward a 20% Efficiency Low-Cost Solid-State Mesoscopic Solar Cell. *J. Phys. Chem. Lett.* **2013**, *4*, 2423−2429.
(5) Li, W.; Li, J.; Wang, L.; Niu, G.; Gao, R.; Qiu, Y. Post Modification of Perovskite Sensitized Solar Cells by Aluminum Oxide for Enhanced Performance. *J. Mater. Chem. A* **2013**, *1*, 11735−11740.
(6) Rhee, J. H.; Chung, C.-C.; Diau, E. W.-G. A Perspective of Mesoscopic Solar Cells Based on Metal Chalcogenide Quantum Dots and Organometal−Halide Perovskites. *NPG Asia Mater.* **2013**, *5*, e68.
(7) Stranks, S. D.; Eperon, G. E.; Grancini, G.; Menelaou, C.; Alcocer, M. J. P.; Leijtens, T.; Herz, L. M.; Petrozza, A.; Snaith, H. J. Electron-Hole Diffusion Lengths Exceeding 1 Micrometer in an Organometal Trihalide Perovskite Absorber. *Science* **2013**, *342*, 341−344.
(8) Xing, G.; Mathews, N.; Sun, S.; Lim, S. S.; Lam, Y. M.; Graetzel, M.; Mhaisalkar, S.; Sum, T. C. Long-Range Balanced Electron- and Hole-Transport Lengths in Organic−Inorganic $CH_3NH_3PbI_3$. *Science* **2013**, *342*, 344−347.
(9) Liang, P. W.; Liao, C. Y.; Chueh, C. C.; Zuo, F.; Williams, S. T.; Xin, X. K.; Lin, J. J.; Jen, A. K. Y. Additive Enhanced Crystallization of Solution-Processed Perovskite for Highly Efficient Planar-Heterojunction Solar Cells. *Adv. Mater.* **2014**, *26*, 3748−3754.
(10) Lotsch, B. V. New Light on an Old Story: Perovskites Go Solar. *Angew. Chem., Int. Ed.* **2014**, *53*, 635−637.
(11) Seo, J.; Park, S.; Kim, Y. C.; Jeon, N. J.; Noh, J. H.; Yoon, S. C.; Sang, S. I. Benefits of Very Thin PCBM and LiF Layers for Solution-Processed p-i-n Perovskite Solar Cells. *Energy Environ. Sci.* **2014**, *7*, 2642−2646.
(12) Lin, Q.; Armin, A.; Nagiri, R. C. R.; Burn, P. L.; Meredith, P. Electro-Optics of Perovskite Solar Cells. *Nat. Photonics* **2015**, *9*, 106−112.
(13) Pang, S.; Hu, H.; Zhang, J.; Lv, S.; Yu, Y.; Wei, F.; Qin, T.; Xu, H.; Liu, Z.; Cui, G. $NH_2CH{=}NH_2PbI_3$: An Alternative Organolead Iodide Perovskite Sensitizer for Mesoscopic Solar Cells. *Chem. Mater.* **2014**, *26*, 1485−1491.
(14) Chen, Q.; Zhou, H.; Hong, Z.; Luo, S.; Duan, H.-S.; Wang, H.-H.; Liu, Y.; Li, G.; Yang, Y. Planar Heterojunction Perovskite Solar Cells via Vapor-Assisted Solution Process. *J. Am. Chem. Soc.* **2014**, *136*, 622−625.
(15) Jung, H. S.; Park, N.-G. Perovskite Solar Cells: From Materials to Devices. *Small* **2015**, *11*, 10−25.
(16) Zhou, H. P.; Chen, Q.; Li, G.; Luo, S.; Song, T. B.; Duan, H. S.; Hong, Z. R.; You, J. B.; Liu, Y. S.; Yang, Y. Interface Engineering of Highly Efficient Perovskite Solar Cells. *Science* **2014**, *345*, 542−546.

DOI: 10.1021/acsami.5b00468
ACS Appl. Mater. Interfaces 2015, 7, 6230−6237

(17) Im, J.-H.; Lee, C.-R.; Lee, J.-W.; Park, S.-W.; Park, N.-G. 6.5% Efficient Perovskite Quantum-Dot-Sensitized Solar Cell. *Nanoscale* **2011**, *3*, 4088−4093.
(18) Chung, I.; Lee, B.; He, J.; Chang, R. P. H.; Kanatzidis, M. G. All-Solid-State Dye-Sensitized Solar Cells with High Efficiency. *Nature* **2012**, *485*, 486−498.
(19) Kim, H.-S.; Lee, C.-R.; Im, J.-H.; Lee, K.-B.; Moehl, T.; Marchioro, A.; Moon, S.-J.; Humphry-Baker, R.; Yum, J.-H.; Moser, J. E.; Graetzel, M.; Park, N.-G. Lead Iodide Perovskite Sensitized All-Solid-State Submicron Thin Film Mesoscopic Solar Cell with Efficiency Exceeding 9%. *Sci. Rep.* **2012**, *2*, 591.
(20) Lee, M. M.; Teuscher, J.; Miyasaka, T.; Murakami, T. N.; Snaith, H. J. Efficient Hybrid Solar Cells Based on Meso-Superstructured Organometal Halide Perovskites. *Science* **2012**, *338*, 643−647.
(21) Burschka, J.; Pellet, N.; Moon, S.-J.; Humphry-Baker, R.; Gao, P.; Nazeeruddin, M. K.; Graetzel, M. Sequential Deposition as a Route to High-Performance Perovskite-Sensitized Solar Cells. *Nature* **2013**, *499*, 316−320.
(22) Heo, J. H.; Im, S. H.; Noh, J. H.; Mandal, T. N.; Lim, C.-S.; Chang, J. A.; Lee, Y. H.; Kim, H.-j.; Sarkar, A.; Nazeeruddin, M. K.; Graetzel, M.; Seok, S. I. Efficient Inorganic−Organic Hybrid Heterojunction Solar Cells Containing Perovskite Compound and Polymeric Hole Conductors. *Nat. Photonics* **2013**, *7*, 487−492.
(23) Hodes, G. Perovskite-Based Solar Cells. *Science* **2013**, *342*, 317−318.
(24) Stoumpos, C. C.; Malliakas, C. D.; Kanatzidis, M. G. Semiconducting Tin and Lead Iodide Perovskites with Organic Cations: Phase Transitions, High Mobilities, and Near-Infrared Photoluminescent Properties. *Inorg. Chem.* **2013**, *52*, 9019−9038.
(25) Edri, E.; Kirmayer, S.; Henning, A.; Mukhopadhyay, S.; Gartsman, K.; Rosenwaks, Y.; Hodes, G.; Cahen, D. Why Lead Methylammonium Tri-Iodide Perovskite-Based Solar Cells Require a Mesoporous Electron Transporting Scaffold (but Not Necessarily a Hole Conductor). *Nano Lett.* **2014**, *14*, 1000−1004.
(26) Gonzalez-Pedro, V.; Juarez-Perez, E. J.; Arsyad, W.-S.; Barea, E. M.; Fabregat-Santiago, F.; Mora-Sero, I.; Bisquert, J. General Working Principles of $CH_3NH_3PbX_3$ Perovskite Solar Cells. *Nano Lett.* **2014**, *14*, 888−893.
(27) Kwon, Y. S.; Lim, J.; Yun, H.-J.; Kim, Y.-H.; Park, T. A Diketopyrrolopyrrole-Containing Hole Transporting Conjugated Polymer for Use in Efficient Stable Organic−Inorganic Hybrid Solar Cells Based on a Perovskite. *Energy Environ. Sci.* **2014**, *7*, 1454−1460.
(28) Mei, A.; Li, X.; Liu, L.; Ku, Z.; Liu, T.; Rong, Y.; Xu, M.; Hu, M.; Chen, J.; Yang, Y.; Grätzel, M.; Han, H. A Hole-Conductor-Free, Fully Printable Mesoscopic Perovskite Solar Cell with High Stability. *Science* **2014**, *345*, 295−298.
(29) http://www.nrel.gov/ncpv/images/efficiency_chart.jpg.
(30) Xiao, J. Y.; Shi, J. J.; Li, D. M.; Meng, Q. B. Perovskite Thin-Film Solar Cell: Excitation in Photovoltaic Science. *Sci. China Chem.* **2015**, *58*, 221−238.
(31) Chiang, C. H.; Tseng, Z. L.; Wu, C. G. Planar Heterojunction Perovskite/$PC_{71}BM$ Solar Cells with Enhanced Open-Circuit Voltage via a (2/1)-Step Spin-Coating Process. *J. Mater. Chem. A* **2014**, *2*, 15897−15903.
(32) Eperon, G. E.; Burlakov, V. M.; Docampo, P.; Goriely, A.; Snaith, H. J. Morphological Control for High Performance, Solution-Processed Planar Heterojunction Perovskite Solar Cells. *Adv. Funct. Mater.* **2014**, *24*, 151−157.
(33) Zhang, H.; Azimi, H.; Hou, Y.; Ameri, T.; Przybilla, T.; Spiecker, E.; Kraft, M.; Scherf, U.; Brabec, C. J. Improved High-Efficiency Perovskite Planar Heterojunction Solar Cells via Incorporation of a Polyelectrolyte Interlayer. *Chem. Mater.* **2014**, *26*, 5190−5193.
(34) Wang, F. Z.; Tan, Z. A.; Dai, S. Y.; Li, Y. F. Recent Advances in Planar Heterojunction Organic−Inorganic Hybrid Perovskite Solar Cells. *Acta Phys. Sin.* **2015**, *64*, 038401.
(35) Li, Y. F.; Zou, Y. P. Conjugated Polymer Photovoltaic Materials with Broad Absorption Band and High Charge Carrier Mobility. *Adv. Mater.* **2008**, *20*, 2952−2958.
(36) Thompson, B. C.; Frechet, J. M. J. Organic Photovoltaics: Polymer−Fullerene Composite Solar Cells. *Angew. Chem., Int. Ed.* **2008**, *47*, 58−77.
(37) Krebs, F. C. Fabrication and Processing of Polymer Solar Cells: A Review of Printing and Coating Techniques. *Sol. Energy Mater. Sol. Cells* **2009**, *93*, 394−412.
(38) Li, Y. F. Molecular Design of Photovoltaic Materials for Polymer Solar Cells: Toward Suitable Electronic Energy Levels and Broad Absorption. *Acc. Chem. Res.* **2012**, *45*, 723−733.
(39) Heeger, A. J. 25th Anniversary Article: Bulk Heterojunction Solar Cells: Understanding the Mechanism of Operation. *Adv. Mater.* **2014**, *26*, 10−28.
(40) Liu, M.; Johnston, M. B.; Snaith, H. J. Efficient Planar Heterojunction Perovskite Solar Cells by Vapour Deposition. *Nature* **2013**, *501*, 395−398.
(41) Kim, H. S.; Park, N. G. Parameters Affecting *I*−*V* Hysteresis of $CH_3NH_3PbI_3$ Perovskite Solar Cells: Effects of Perovskite Crystal Size and Mesoporous TiO_2 layer. *J. Phys. Chem. Lett.* **2014**, *5*, 2927−2934.
(42) Jeng, J.-Y.; Chiang, Y.-F.; Lee, M.-H.; Peng, S.-R.; Guo, T.-F.; Chen, P.; Wen, T.-C. $CH_3NH_3PbI_3$ Perovskite/Fullerene Planar-Heterojunction Hybrid Solar Cells. *Adv. Mater.* **2013**, *25*, 3727−3732.
(43) Wang, K.-C.; Jeng, J.-Y.; Shen, P.-S.; Chang, Y.-C.; Diau, E. W.-G.; Tsai, C.-H.; Chao, T.-Y.; Hsu, H.-C.; Lin, P.-Y.; Chen, P.; Guo, T.-F.; Wen, T.-C. *p*-Type Mesoscopic Nickel Oxide/Organometallic Perovskite Heterojunction Solar Cells. *Sci. Rep.* **2014**, *4*, 4756.
(44) Wu, Y. Z.; Islam, A.; Yang, X. D.; Qin, C. J.; Liu, J.; Zhang, K.; Peng, W. Q.; Han, L. Y. Retarding the Crystallization of PbI_2 for Highly Reproducible Planar-Structured Perovskite Solar Cells via Sequential Deposition. *Energy Environ. Sci.* **2014**, *7*, 2934−2938.
(45) Xiao, M. D.; Huang, F. Z.; Huang, W. C.; Dkhissi, Y.; Zhu, Y.; Etheridge, J.; Gray-Weale, A.; Bach, U.; Cheng, Y. B.; Spiccia, L. A Fast Deposition−Crystallization Procedure for Highly Efficient Lead Iodide Perovskite Thin-Film Solar Cells. *Angew. Chem., Int. Ed.* **2014**, *53*, 9898−9903.
(46) Shi, J.; Dong, J.; Lv, S.; Xu, Y.; Zhu, L.; Xiao, J.; Xu, X.; Wu, H.; Li, D.; Luo, Y.; Meng, Q. Hole-Conductor-Free Perovskite Organic Lead Iodide Heterojunction Thin-Film Solar Cells: High Efficiency and Junction Property. *Appl. Phys. Lett.* **2014**, *104*, 063901.
(47) Min, J.; Zhang, Z.-G.; Hou, Y.; Ramirez Quiroz, C. O.; Przybilla, T.; Bronnbauer, C.; Guo, F.; Forberich, K.; Azimi, H.; Ameri, T.; Spiecker, E.; Li, Y.; Brabec, C. J. Interface Engineering of Perovskite Hybrid Solar Cells with Solution-Processed Perylene−Diimide Heterojunctions toward High Performance. *Chem. Mater.* **2014**, *27*, 227−234.
(48) Brabec, C. J.; Shaheen, S. E.; Winder, C.; Sariciftci, N. S.; Denk, P. Effect of LiF/Metal Electrodes on the Performance of Plastic Solar Cells. *Appl. Phys. Lett.* **2002**, *80*, 1288−1290.
(49) Sun, K.; Chang, J.; Isikgor, F. H.; Li, P.; Ouyang, J. Efficiency Enhancement of Planar Perovskite Solar Cells by Adding Zwitterion/LiF Double Interlayers for Electron Collection. *Nanoscale* **2015**, *7*, 896−900.
(50) Gao, D.; Helander, M. G.; Wang, Z. B.; Puzzo, D. P.; Greiner, M. T.; Lu, Z. H. C_{60}:LiF Blocking Layer for Environmentally Stable Bulk Heterojunction Solar Cells. *Adv. Mater.* **2010**, *22*, 5404−5408.
(51) Liu, X. D.; Lee, J. Y.; Guo, L. J. Efficiency and Stability Enhancement of Polymer Solar Cells using Multi-Stacks of C_{60}/LiF as Cathode Buffer Layer. *Org. Electron.* **2013**, *14*, 469−474.
(52) Yip, H. L.; Hau, S. K.; Baek, N. S.; Ma, H.; Jen, A. K. Y. Polymer Solar Cells That Use Self-Assembled-Monolayer-Modified ZnO/Metals as Cathodes. *Adv. Mater.* **2008**, *20*, 2376−2382.
(53) Trevisan, R.; Döbbelin, M.; Boix, P. P.; Barea, E. M.; Tena-Zaera, R.; Mora-Seró, I.; Bisquert, J. PEDOT Nanotube Arrays as High Performing Counter Electrodes for Dye Sensitized Solar Cells. Study of the Interactions Among Electrolytes and Counter Electrodes. *Adv. Energy Mater.* **2011**, *1*, 781−784.
(54) Ecker, B.; Egelhaaf, H. J.; Steim, R.; Parisi, J.; von Hauff, E. Understanding S-Shaped Current−Voltage Characteristics in Organic Solar Cells Containing a TiO_x Interlayer with Impedance Spectros-

DOI: 10.1021/acsami.5b00468
ACS Appl. Mater. Interfaces 2015, 7, 6230−6237

copy and Equivalent Circuit Analysis. *J. Phys. Chem. C* **2012**, *116*, 16333−16337.
(55) Yan, L.; Song, Y.; Zhou, Y.; Song, B.; Li, Y. F. Effect of PEI Cathode Interlayer on Work Function and Interface Resistance of ITO Electrode in the Inverted Polymer Solar Cells. *Org. Electron.* **2015**, *17*, 94−101.

DOI: 10.1021/acsami.5b00468
ACS Appl. Mater. Interfaces 2015, 7, 6230−6237